Multi-bead overlapping model with varying cross-section profile for robotic GMAW-based additive manufacturing

Zeqi Hu[1,2,3] · Xunpeng Qin[1,2,3] · Yifeng Li[1,2,3] · Jiuxin Yuan[1,2,3] · Qiang Wu[1,2,3]

Abstract

In robotic GMAW-based additive manufacturing, the surface evenness of the deposited layer was significant to the dimensional accuracy and the stable fabrication process, and it was determined by the multi-bead overlapping distance. To obtain the optimal overlapping distance, a group of two-bead overlapping experiments was conducted with different overlapping ratio. The cross-section shape was observed and the variation of the bead profile caused by the damming up of the previous bead was investigated. The second bead profile could be fitted by a rotated varying parabola or circular arc function with the decreasing of the overlapping distance from the initial single bead width (w) to 0. A varying cross-section profile overlapping model was developed based on the actual forming characteristics of the overlapping experiment, through which the varying profile of two overlapping beads with arbitrary distance could be predicted. Then, the optimal overlapping distance was calculated under some principles to achieve a relatively flat top surface and stable overlapping process, and the multi-bead overlapping experiments were performed to validate the model. The results showed that the model could achieve an excellent approximation to the actual overlapping experiment, and the good surface evenness and stable overlapping process was obtained, which was significant to the research into the appearance optimization in GMAW-based additive manufacturing.

Keywords Additive manufacturing · Gas metal arc welding · Bead overlapping model · Varying cross-section profile

Introduction

Additive manufacturing of metal parts is increasingly popular in recent decades. The components with complex structure could be fabricated through a direct near-net shape method with the material deposited layer upon layer. It has a high material utilization and simple process compared with the traditional subtractive manufacturing technology (Jiang et al. 2019a; Yang et al. 2016; Zhang et al. 2017). There are several different kinds of heat source (Jhavar et al. 2014; Roberts et al. 2009; Xiong et al. 2009) applied in the additive manufacturing, such as laser, plasma arc, electron beams, and gas metal arc welding (GMAW). Laser was the most widely used heat source with a high surface accuracy, fine microstructure and good mechanical properties, but the deposition efficiency was low and the cost of the equipment (e.g. semiconductor laser unit) was expensive (Gu et al. 2012; Weng et al. 2019). The traditional GMAW was widely applied in the material joining or tool repairing and maintenance, but recently the GMAW-based additive manufacturing technology is especially concerned for the low equipment cost, high deposition efficiency (Cunningham et al. 2018; Las-Casas et al. 2018), good mechanical properties and flexible automation integration (Panda et al. 2019; Williams et al. 2016).

During the process of GMAW-based additive manufacturing, the slicing and path planning should be conducted firstly with a certain layer thickness and adjacent bead overlapping distance (Ding et al. 2015; Jiang et al. 2019b). For the disperse layer stacking method, the stair-stepping effect (Ding et al. 2018) is inevitable, and a larger layer thickness would result in a rougher surface appearance. At present, the algorithm of uniform layer thickness slicing is widely used, which made the part surface coarse especially at the position of flat slope. Zheng et al. (2018) proposed a method for

✉ Xunpeng Qin
qxp915@hotmail.com

1 School of Automotive Engineering, Wuhan University of Technology, Wuhan 430070, China

2 Hubei Key Laboratory of Advanced Technology for Automotive Components, Wuhan 430070, China

3 Hubei Collaborative Innovation Center for Automotive Components Technology, Wuhan 430070, China

slicing three-dimensional CAD models based on the posture of voxels of two-photon polymerization (TPP) so that the stair-stepping effect could be remitted and the number of layers could be optimized.

Moreover, the deposited layer was obtained through the overlapping of many parallel beads, and the research of optimal bead overlapping distance for adjacent beads has been attracting much attention. The weld bead cross-section profile is a curve that could be approximated by a parabola, cosine or circular arc, instead of the rectangle (Ghanty et al. 2007). Therefore, it is difficult to obtain the desired bead overlapping distance that achieved the flat layer top surface. The overly long distance between the adjacent weld beads would result in the deep valley and uneven layer surface, while the overly short distance would lead to the heaping up of the filler material, both of which would affect the dimensional accuracy and the processing efficiency, and even lead to the failure of the deposition. For the improper overlapping distance, the actual building height would be greater or shorter than the predefined layer thickness, so that the deposition head (welding gun) would get closer or farther to the top surface of the existing layers, which would result in the overly long contact tip to work distance or a collision.

To investigate the forming characteristics of the GMAW, some researchers (Bai et al. 2018; Cho et al. 2019; Hu et al. 2008, 2018; Lei et al. 2018; Prajadhiama et al. 2019; Zhou et al. 2016) built the numerical model or physical model considering the weld pool dynamics, droplets impingement, surface tension, arc plasma pressure, electromagnetic force, marangoni effect, latent heat, heat and mass transfer and other physic phenomenon with the FEM or CFD method. The thermal distribution, weld pool profile, residual stress and distortion, single bead geometry were simulated and the influence of the different parameters was analyzed. However, the physical metallurgical process of the GMAW was extremely complicated, so that the mathematical representation and the physical modeling were intricate and the numerical computation of the CFD or the FEM method was heavy and hard to reach the convergence. Although the penetration of the welding process could be observed through the simulated thermal profile and the weld pool where the temperature exceeded the melting point, the accurate profile curve of the bead reinforcement was hard to obtain. Thus, only one or two beads welding process was simulated, and it is hard to investigate the multi-bead multi-layer additive manufacturing process.

Besides, some analytical mathematic model based on the experiment observation with a relative low computation was developed. Suryakumar et al. (2011) assumed that the bead profile was a symmetrical parabola curve, and proposed a flat-top overlapping model (FOM) to optimize the smoothness of the layer top surface, and the results showed that the optimal overlapping distance was 2/3 of the bead width (w).

Through preliminary experiment, Cao et al. (2011) found that the sine function could fit the actual weld bead profile best, and presented that the optimum-overlapping coefficient should be 63.66% of the bead width, through the identical FOM model. Xiong et al. (2013) analyzed the bead cross-section function model and the ratio of the wire feed rate to the welding speed (WSR), and found that the cross-section profile could be fitted by the circular arc or parabola with different WSR. Then the optimal overlapping distance was calculated through the FOM model. The FOM model was based on the assumption that the single bead section profile is a certain curve function, and the weld bead shape remains unchanged during the overlapping of the adjacent beads. However, because of the heat accumulation, the spreading effect and the damming up of the existing bead, the fluid flow in the weld pool of the second bead would be different from the first one, so that the second bead shape would be different. Ding et al. (2015) developed a tangent overlapping model (TOM) in which the critical valley between the adjacent beads was approximated through a line that was tangent to the second bead. The optimal overlapping distance was calculated as 0.738 w with the single bead profile represented by the parabola model. For this model, when the step over increment exceeded the optimal distance, the second bead height increased, otherwise the second bead shape remained unchanged. Li et al. (2018) proposed a layers-overlapping strategy for multi-layer multi-bead components with homogeneous layers, which overcome the bead spreading at the edge of the layer through the adjustment of the bead overlapping distance and the torch welding speed. Although the weld pool spreading effect and the material shortage were considered to achieve a homogeneous layer, the process was quite complicated, which was not suitable for the continuous and efficient fabrication.

Therefore, in this paper, the varying profile of the second bead was considered. Firstly, a group of preliminary two-bead overlapping experiments with different overlapping distance was conducted, and the profile was measured. The shape deformation and characteristics resulted from the spreading effect and damming up of the first bead was analyzed. Then, a mathematic varying profile multi-bead overlapping model (VOM) considering the gradually changing shape of the second bead was developed and validated through experiments, so that the shape of the second bead could be described and predicted by an equation. Finally, the optimal overlapping distance to achieve a smooth layer surface was then calculated based on the proposed VOM model. Compared with the FEM or CFD physical model, the proposed mathematic model requires less computation and the in-depth understanding of the AM process, such as heat transfer and mechanics of materials. Although extensive preliminary experimental works were needed to establish the model, the accurate bead geometry could be obtained

with an arbitrary multi-bead overlapping ratio, and based on which the optimal overlapping distance could be calculated to achieve the flat layer surface and stable overlapping process.

The content of this paper was organized as follows: the experiment setup and the two-bead overlapping experiment details were presented in Sect. 2; the forming characteristics of two-bead overlapping process and the derivation of the varying profile multi-bead overlapping model (VOM) were described in Sect. 3; the optimization of the overlapping distance was issued in Sect. 4, and the results of validation experiment and discussion were addressed in the final Sect. 5.

Preliminary overlapping experiment

Experimental setup

The GMAW-based additive manufacturing system was illustrated in Fig. 1. The six-axis ABB IRB 1410 industrial robot and the LORCH S8 welding supply were applied to perform the welding process along the predefined welding path. The welding mode was the direct current electrode positive (DCEP) gas metal arc welding (GMAW), and the arc voltage and wire feed speed could be adjusted respectively. The Creaform Handy Scan700 3D laser scanner with a spatial accuracy of 0.03 mm was applied to measure the three-dimensional shape of the weld bead.

The welding experiment was performed on a mild steel substrate (300 mm × 200 mm × 10 mm), which was clamped to avoid the deformation caused by the welding thermal stress. The filler material was AWS ER70S-6 solid wire of 1.2 mm diameter with a composition C (0.06–0.15%), Mn (1.40–1.85%), Si (0.8–1.15%), Ni ($\leq$0.15%), and Cr ($\leq$0.15). The shielding gas was a mixture of 18% CO_2 and 82% Ar with a flow rate of 15 L/min. The welding process

was controlled through the robot controller which connected the robot actuator and the welding power source, with the ABB Rapid code containing the movement instruction and the welding instruction. After the weld bead was deposited, the points cloud representing the bead geometry was obtained through the 3D laser scanner. The data was processed in the commercial software Geomagic Studio and MATLAB to obtain the weld bead cross section profile.

Two-bead overlapping experiment

Firstly, to analyze the shape of the single weld bead, a welding deposition experiment on the flat substrate was conducted, and the welding process parameters employed in this study were given as the wire feed speed (WFS) at 5.0 m/min, the arc voltage (AV) at 22.0 V, the torch travel speed (TTS) at 6.0 mm/s, the contact tip to workpiece distance (CTWD) at 8.0 mm, and the torch was maintained perpendicular to the flat substrate. The arc current with this welding parameters configuration was 196 A. The bead shape was measured through the 3D laser scanner, and the bead cross section profile consisted of a series of two-dimensional points with *X/Y* coordinates was extracted. According to the previous study (Ding et al. 2015), good agreement between experimental results and the parabola model was obtained under various welding parameters, therefore, in this paper, the bead cross-section profile was fitted by the parabola function as is expressed with Eq. (1).

$$y = a(x + b)^2 + c \tag{1}$$

where a, b, c were the coefficients, and $a = -0.1354$, $b = -4.6152$, $c = 2.5078$. The square of the correlation between the actual value and the predicted value ($R^2 = 0.9927$) and the root-mean-square error ($RSME = 0.0710$) were used to represent the goodness of the fitting function. The fitting curve and the actual bead profile were illustrated in Fig. 2. It was observed that the
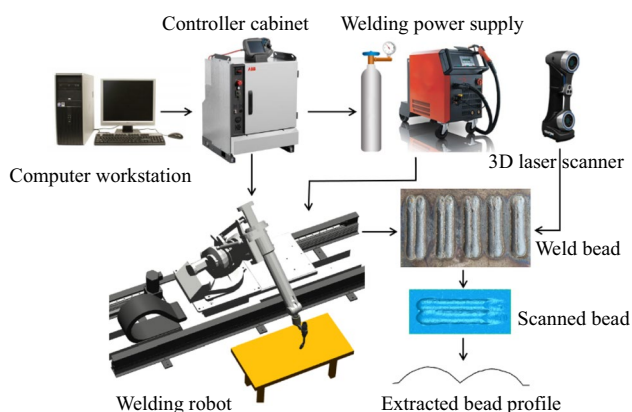

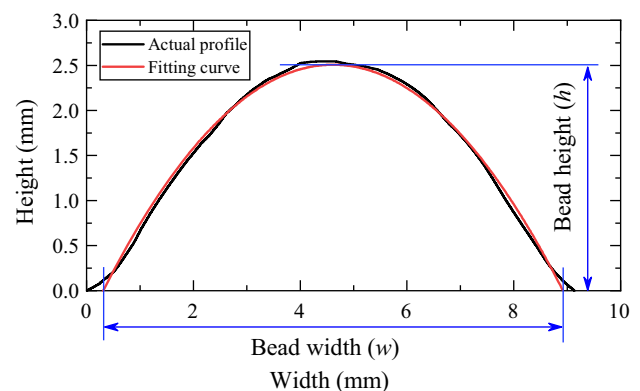**Fig. 1** The GMAW-based additive manufacturing system

Fig. 2 The fitting curve and the cross section profile of the actual bead

parabolic fitting curve could approximate the actual weld bead profile with a high accuracy, except for the slight deviation at the toe of the bead, which was caused by the smoothing effect of the 3D scanner at the sharp corners. Therefore, as is illustrated in Fig. 2, the bead width (w) and height (h) could be calculated through the coefficients as the following Eq. (2), and for the selected welding parameters, $w = 8.6$ mm, $h = 2.5$ mm.

$$w = 2\sqrt{-c/a}$$
$$h = c \tag{2}$$

To investigate the second bead forming characteristics during the multi-bead overlapping process, a group of two-bead overlapping experiments were conducted on the flat substrate, with the overlapping distance (d_o) and the overlapping ratio (η, $d_o = \eta w$) listed in Table 1. The first bead was deposited under the ambient temperature of 25 °C, and before the deposition of the second bead, the substrate was cooled down to the initial temperature to avoid the influence of the heat accumulation on the bead forming. Then, the bead cross-section profiles in 10 experiments were extracted and aligned, as is shown in Fig. 3. The vertical lines labeled 0, 1, 2 to 10 were the central line of the weld bead in corresponding to the overlapping distance, respectively. It can be found that all the cross-section profiles consisted of two convex curves representing the overlapping of two beads. The shape of the first bead in all groups remained consistent, while the second bead gradually changed with different overlapping distance, and the height of the second bead increased with the decreasing of the overlapping distance. For the

experiment No. 1, the overlapping distance ($d_o = 1.05w$) was greater than the single weld bead width (w), so there was no overlapping region between the adjacent beads, and the shape of the second bead was the same with the first one. When $d_o < w$, there existed overlapping region between the adjacent beads. Because of the damming up of the first bead, the molten metal fluid of the second bead was different from the conditions in the first bead, and thus the bead shape transformed. Besides, for different overlapping distance, the profile at the valley between the adjacent beads is a curve rather than a line tangent to the second bead profile.

The second bead width was also measured. As is shown in Fig. 3, $A_{10}B_{10}$ is the chord length of the second bead profile representing the width of the second bead corresponding to the experiment No. 10, A_9B_9 represented the width of the second bead in No. 9, and so forth. The second bead width in the overlapping experiment was depicted in Fig. 4, and it can be found that the change of the second bead width in the overlapping group was not significant, and the value was close to the single bead width. Besides, when the overlapping distance was zero, the second bead was completely piled on the first one, so that the second bead width was equal to the single bead width; when the overlapping distance was greater than the single bead width, there is no overlapping region, so that the second bead width was equal to the single one. Therefore, it can be concluded that during the two-bead overlapping process the second bead width represented by the profile chord length was equal to the single bead width and remained unchanged, while the shape of the second bead varied gradually.
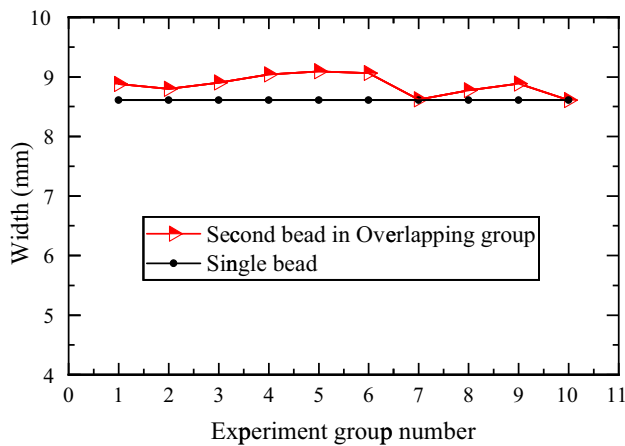
Moreover, for all the weld beads, the area of the cross section could be calculated as $A = \pi d^2 v_w \mu / 4 v_T$, where d

Table 1 The two-bead overlapping distance

No.	10	9	8	7	6	5	4	3	2	1
Ratio (η)	0.11	0.21	0.32	0.42	0.53	0.63	0.74	0.84	0.95	1.05
Distance (mm)	0.91	1.81	2.72	3.63	4.54	5.44	6.35	7.26	8.16	9.07
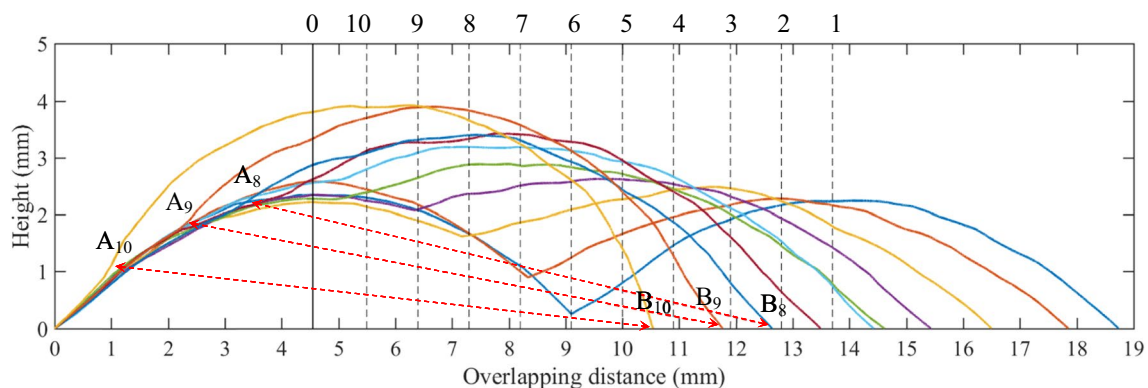
Fig. 3 The cross-section profile in the two-bead overlapping experiments

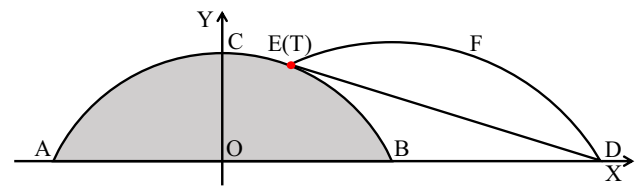**Fig. 4** The second bead width in the overlapping experiments

Fig. 5 The diagram of two-bead overlapping model at the tangency point ($\eta = \eta_T$)

4. When $d_o < \eta_T w$, the second bead profile could be represented by a circular arc function.
5. The chord length of the second bead profile was equal to the single bead width and remained unchanged.
6. The area of the weld bead cross-section remained consistent.

was the wire diameter, v_w was the wire feed speed, μ was the wire utilization rate, and v_T was the torch travel speed. The welding process parameters remained unchanged, so that the area of the second bead was consistent with the first one. For the No. 1, 2, 3, 4 and 5 experiments, it can be observed that the shape of the second bead profile could be approximated by a rotated parabola function; while for the No. 6, 7, 8, 9 and 10 group, the shape of the second bead was more similar to a rotated circular arc curve. Therefore, an assumption was made to reflect the varying of the second bead shape. Namely, when the chord of the second bead profile was tangent to the first parabolic bead profile, the overlapping ratio was η_T, and the intersection of the chord line with the first bead profile was the defined as the tangency point; when $\eta \geq \eta_T$, the second bead profile was approximated by a parabola function with the certain new coefficients; when $\eta < \eta_T$, the second bead profile was represented by a circular arc function.

Thus, the single weld bead model and two-bead overlapping model could be developed based on the above principles.

Firstly, the single bead profile model could be expressed by the following equation:

$$y = ax^2 + b \quad (a = -4h/w^2, b = h) \tag{3}$$

where a, b was the coefficients. To simplify the mathematical representation and visualization process, the parabola function was set symmetrical about the Y-axis. The diagram of two-bead overlapping model at the tangency point is depicted in Fig. 5. The region AOBC was the first bead, EBDF was the second bead. The line DE was the chord of the second bead profile which was tangent to the parabolic curve ACB at the tangency point T(E). To calculate the overlapping ratio at the tangency point η_T, the equations could be developed based on the two conditions:

1. The chord length of second bead profile DE was equal to the first bead width AB (w), and it could be expressed by the following equations:

Multi-bead overlapping modeling

Tangency point of the parabolic curve

According to the two-bead overlapping experiment and the investigation of the forming characteristics, the principles for the forming of two-bead overlapping process could be summarized as follows:

1. The profile of the single weld bead could be fitted by a parabola function.
2. The shape of the second bead changed with different overlapping distance.
3. When $d_o \geq \eta_T w$, the second bead profile was approximated by a parabola function.

$$\begin{cases} x_D = w/2 + \eta_T w \\ y_D = 0 \\ y_E = ax_E^2 + b \\ \sqrt{(x_D - x_E)^2 + (y_D - y_E)^2} = w \end{cases} \tag{4}$$

where x_D, y_D, x_E and y_E was the X/Y coordinate of the point D and E, respectively.

2. The line DE was tangent to the curve $\overset{\frown}{ACB}$ at point E, i.e., the slope of ACB parabolic function at point E was equal to that of line DE, and it could be represented by the following equation:

$$\frac{dy}{dx}\bigg|_{x=x_E} = 2ax_E = \frac{y_D - y_E}{x_D - x_E} \tag{5}$$

The system of nonlinear equations could be established by the combination of Eqs. (4) and (5), and only x_E, η_T were the unknown variables. The equations system could be solved through the numerical method "Trust-Region-Dogleg" (Sheng et al. 2018) with MATLAB code. For the selected welding process parameters, $w = 8.6$ mm, $h = 2.5$ mm, the solution was calculated that $x_E = 1.0508$, $\eta_T = 0.5841$.

Overlapping distance $d_o \geq \eta_T w$

When the overlapping distance $d_o \geq \eta_T w$, the second bead profile was approximated by a parabola function with the new coefficients. As is shown in Fig. 6, the chord line DE was no longer tangent to the parabolic curve ACB. The point E lay on the curve before the tangency point T, and the point G was the intersection of the extension of line DE and the curve ACB. The line EI, GH were perpendicular to line AB, and line FJ was perpendicular to ED, representing the height (h_2) of the second bead parabolic model. In this circumstance, the overlapping ratio η was predefined, and the intersection point between the second and first bead profile was unknown, which could be solved from the known variables.

Firstly, the coordinates of point E (x_E, y_E) could be solved based on the condition that the second bead chord length DE was equal to the width of the first bead (w). The equations were shown as follows:

Fig. 6 The schematic diagram of two-bead overlapping model when $d_o \geq \eta_T w$

$$\begin{cases} x_D = w/2 + \eta w \\ y_D = 0 \\ y_E = ax_E^2 + b \\ \sqrt{(x_D - x_E)^2 + (y_D - y_E)^2} = w \end{cases} \Rightarrow \begin{cases} x_E \\ y_E \end{cases} \tag{6}$$

Then, the second bead height (h_2) could be solved based on the condition that the area of the second bead cross-section was equal to that of the first bead, and the equations were shown as follows:

$$\begin{cases} S_{ABC} = \int_{-w/2}^{w/2} (ax^2 + b)\, dx = \frac{2}{3}hw \\ S_{IBE} = \int_{x_E}^{w/2} (ax^2 + b)\, dx \\ S_{BDE} = S_{IDE} - S_{IBE} = \frac{ID \cdot IE}{2} - S_{IBE} \\ S_{EFD} = \frac{2}{3}DE \cdot FJ = \frac{2}{3}wh_2 \\ S_{ABC} = S_{BDFE} \Rightarrow S_{ABC} = S_{BDE} + S_{EFD} \end{cases} \tag{7}$$

Based on the calculated x_E, h_2, the profile of the second bead BDFE was determined, and the mathematic expression of the parabolic curve $\overparen{EFD}$ could be obtained through the coordinate transformation (Arvo 1992) from the position $E_1F_1D_1$ to the position EFD, as is shown in Fig. 7. Firstly, the parabolic curve ($E_1F_1D_1$) which was identical with the second bead profile was set at the origin point as is expressed by Eq. (8), and the homogeneous coordinates of the point on the curve could be expressed as $P(x)$. Then the region $E_1F_1D_1$ was translated along the –X direction for a distance of $-w/2$, so that the point D_1 was moved to the origin O. Then the object $E_2F_2D_2$ was rotated around the origin O (D_2) along the clockwise direction to the position $E_3F_3D_3$, and the rotating angle was $\alpha = \angle ODE$. The object $E_3F_3D_3$ was then translated to the position EFD with the distance $\triangle x = \eta w + w/2$. Finally, the coordinates of the point on the curve EFD $P'(x)$ could be expressed as Eq. (9),

Fig. 7 The process of coordinate transformation to obtain the expression of the second bead profile

where $R(x)$ and $T(x)$ was the rotating and translating coordinate transformation matrix.

$$y = a_2 x^2 + b_2$$

$$a_2 = -\frac{4h_2}{w^2}, \quad b_2 = h_2$$

$$P(x) = \begin{bmatrix} x \\ a_2 x^2 + b_2 \\ 1 \end{bmatrix} \tag{8}$$

$$\alpha = \angle ODE = \arctan\left(\frac{y_E}{x_D - x_E}\right)$$

$$R(-\alpha) = \begin{bmatrix} \cos(\alpha) & \sin(\alpha) & 0 \\ -\sin(\alpha) & \cos(\alpha) & 0 \\ 0 & 0 & 1 \end{bmatrix}$$
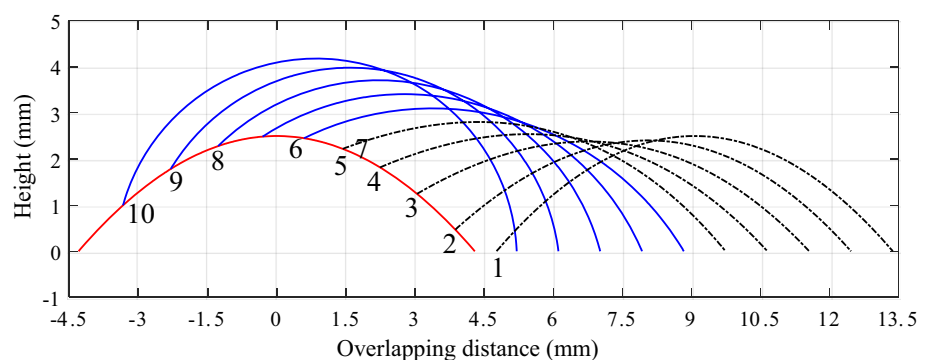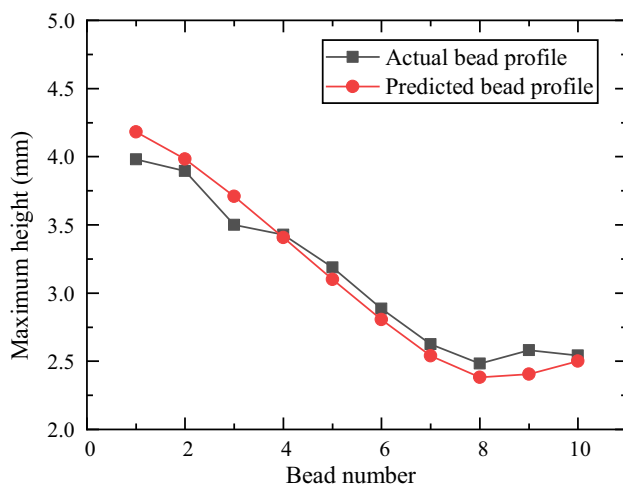
$$T(\triangle x, 0) = \begin{bmatrix} 1 & 0 & \triangle x \\ 0 & 1 & 0 \\ 0 & 0 & 0 \end{bmatrix} \tag{9}$$

$$P'(x) = T(\eta w + w/2, 0) \cdot R(-\alpha) \cdot T(-w/2, 0) \cdot P(x)$$

Fig. 8 The schematic diagram of two-bead overlapping model when $d_o < \eta_T w$

Overlapping distance $d_o < \eta_T w$

When the overlapping distance $d_o < \eta_T w$, the second bead profile was approximated by a circular arc function. As is shown in Fig. 8, point E lay on the parabolic curve behind the tangency point T, and point G was the intersection of the chord line DE and the parabolic curve ACB. The position of point E could be obtained through the same approach as the Eqs. (6), and the coordinates of point G (x_G, y_G) could be solved through the condition that the point G lay on both of line DE and the parabolic curve ACB, as is expressed by the following equations:

$$\begin{cases} y_G = a x_G^2 + b \\ \frac{y_G - y_D}{x_G - x_D} = \frac{y_E - y_D}{x_E - x_D} \end{cases} \Rightarrow \begin{cases} x_G \\ y_G \end{cases} \tag{10}$$

The second bead height h_2 could be solved under the conditions that the area of the second bead cross-section was equal to that of the first bead, and the equations were shown as follows:

$$\begin{cases} S_{ABC} = \int\limits_{-w/2}^{w/2} \left(ax^2 + b\right) dx = \frac{2}{3}hw \\ S_{IHGE} = \frac{(IE + HG) \cdot IH}{2} \\ S_{GCE} = S_{IHGCE} - S_{IHGE} = \int\limits_{x_E}^{x_G} \left(ax^2 + b\right) dx - S_{IHGE} \\ S_{HBG} = \int\limits_{x_G}^{w/2} \left(ax^2 + b\right) dx \\ S_{BDG} = S_{HDG} - S_{HBG} = \frac{HD \cdot HG}{2} - S_{HBG} \end{cases} \tag{11}$$

$$R = \frac{(EJ)^2 + (FJ)^2}{2 \cdot FJ}$$

$$\beta = 2 \arcsin\left(\frac{EJ}{R}\right)$$

$$S_{EFD} = \frac{\beta R^2}{2} - DE \cdot (R - FJ)$$

$$S_{ABC} = S_{ECBDF} \Rightarrow S_{ABC} = S_{EFD} - S_{GCE} + S_{BDG}$$

Fig. 9 The two-bead overlapping model of the 10 experiments with different overlapping ratio

Fig. 10 The maximum height of the predicted bead profile and the actual overlapping model

where R was the radius of the circular arc $\overset{\frown}{EFD}$, and β was the corresponding central angle. The coordinates of the point on the curve $\overset{\frown}{EFD}$ could be expressed through the above mentioned coordinate transformation method. Figure 9 illustrated the two-bead overlapping model corresponding to the No. 1 to 10 experiments, in which the overlapping ratio $\eta \geq \eta_T$, for No. 5, 4, 3, 2 and 1, and $\eta < \eta_T$, for No. 10, 9, 8, 7 and 6. Figure 10 was the maximum height of the predicted model calculated through the proposed two-bead overlapping model and the actual overlapping experiment. The max error was 6.9%, the average error was 3.5%, the area of the second bead was equal to the first bead, and the chord length of the second bead was equal to the width of the first bead. Comparing Fig. 3 with Fig. 9, it was observed that the second profile in the two-bead overlapping model varied gradually with the overlapping distance, and the proposed model was in good agreement with the actual overlapping experiment in experiments No. 1 to 10, for both the shape and the dimension. When the overlapping ratio $\eta \geq \eta_T$, the shape of the cross-section profile was represented by a parabolic curve. Especially when the $\eta \geq 1.0$, there is no overlapping region between the adjacent two beads, and the second bead was absolutely identical with the first one. When the overlapping ratio $\eta < \eta_T$, the second bead was more rounded, because of the damming up effect of the first bead and the

surface tension acting on the fluid in the weld pool, the profile is more similar to a circular arc curve. Overall, the proposed varying profile two-bead overlapping model (VOM) could describe the shape changing of the two-bead overlapping process well, with which the profile of the second bead could be predicted and analyzed through the mathematic equations, instead of the complex actual welding experiment and 3D measuring process.

Overlapping distance optimization

From the preliminary welding experiments and the two-bead overlapping model, it can be found that the shape of the second bead varied gradually. As is illustrated in Fig. 9, the valley between the two adjacent beads existed all the time, but the depth of the valley was different for the diverse overlapping distance. Thus, in this paper, the goal was to optimize the smoothness of the top surface, reduce the unevenness caused by the discontinuous valley, and guarantee the stability of the overlapping process.

The optimal overlapping ratio was assumed as η_b. As is illustrated in Fig. 11, when the overlapping distance was $d_o = \eta_b w$, the valley between the two adjacent beads was small, and the top surface was relatively flat. The multi-bead overlapping process was consistent and stable, and the third, fourth or subsequent bead could be regarded as the duplicating of the second bead, which meant that the shape and dimension reached a stable condition and remained unchanged. Thus, the subsequent bead profile could be obtained through the translation of the second bead profile at the same overlapping distance.

To calculate the optimal overlapping ratio, the conditions could be concluded that:

1. The optimal overlapping ratio was assumed to lay in the region of $d_o \geq \eta_T w$. Thus, the first bead was represented by a parabola function, and the second bead profile was approximated by another rotated parabola function.
2. The chord length of the second bead profile was equal to the width of the first bead, which could be expressed by the Eq. (6).
3. The cross-section area of all weld bead was equivalent, and it could be represented by Eq. (7).

Fig. 11 The schematic diagram of the multi-bead overlapping model for the optimal overlapping ratio
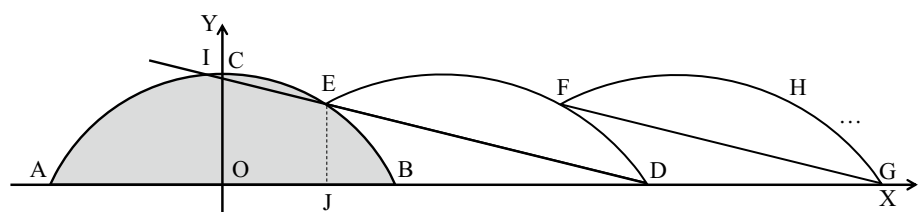
4. The third, fourth and subsequent bead profile was obtained through translation of the second one. Namely, the subsequent bead profile could be expressed by a periodic function $y = \varphi(x) = \varphi(x + T)$, and the period was the optimal overlapping distance $T = d_o = \eta_b w$. The function of curve $\widehat{EFD}$ could be obtained through the coordinates transformation method as expressed by the above Eq. (9), and the point F could be obtained through the translation of point E as is expressed by $P_F = T(\eta_b w, \, 0) \cdot P_E$. Because of the periodicity of the function, the X/Y coordinates of P_F and $P_{\widehat{EFD}}$ should be equivalent respectively, i.e., $P_F.x = P_{\widehat{EFD}}.x$, $P_F.y = P_{\widehat{EFD}}.y$.

The above equations under the conditions (1)–(4) were combined, and the unknown variables were x_E, η_b, h_2 (second bead height), x (initial parameter for points on the curve $\widehat{EFD}$). The numerical method was applied to obtain the solution. For the selected welding parameters, the optimal overlapping ratio was calculated as $\eta_b = 0.6557$, which lay in the region of $d_o \geq \eta_T w$. It can be found that the optimal overlapping ratio was approximate to the FOM model (63.66%), but less than the TOM model ($0.738w$). The multi-bead overlapping process with the optimal distance ($0.6557w$) was

shown in Fig. 12, and all the adjacent beads profile were well connected. The biggest height of the first bead was 2.5 mm, while the biggest height of the subsequent beads was 2.74 mm, and the height at the bottom of the valley was 2.15 mm, so that the subsequent bead height was a little bigger than the first one, but the bead shape was consistent and the continuous overlapping process was stable.

The multi-bead overlapping model with $\eta < 0.6557$ and $\eta > 0.6557$ was also investigated, as is shown in Fig. 13. When $\eta = 0.5$, the overlapping distance was less than the optimal distance, so that excess material was filled into the valley and resulted in the convex hull, and the biggest height of the second bead was 3.18 mm, which was far more than the first bead height. For the third bead, because of the piling up of the excess material resulted from the small overlapping distance, the bead profile would change and the height would increase gradually, and the second bead profile was no longer proper to represent the third one, so that the crossover between the third and second profile appeared, as is shown in Fig. 13a. When $\eta = 0.8$, the overlapping distance was greater than the optimal distance, the valley between the first and second bead was broad and deep. For the third bead, some of the material would be used to fill the broad valley, and the shape of the profile would change, so that the second bead

Fig. 12 The multi-bead overlapping process at the optimal overlapping distance ($\eta_b w$)
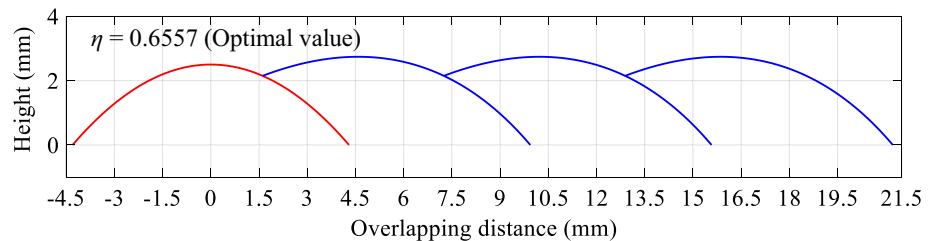
Fig. 13 The multi-bead overlapping process at the non-optimal overlapping distance
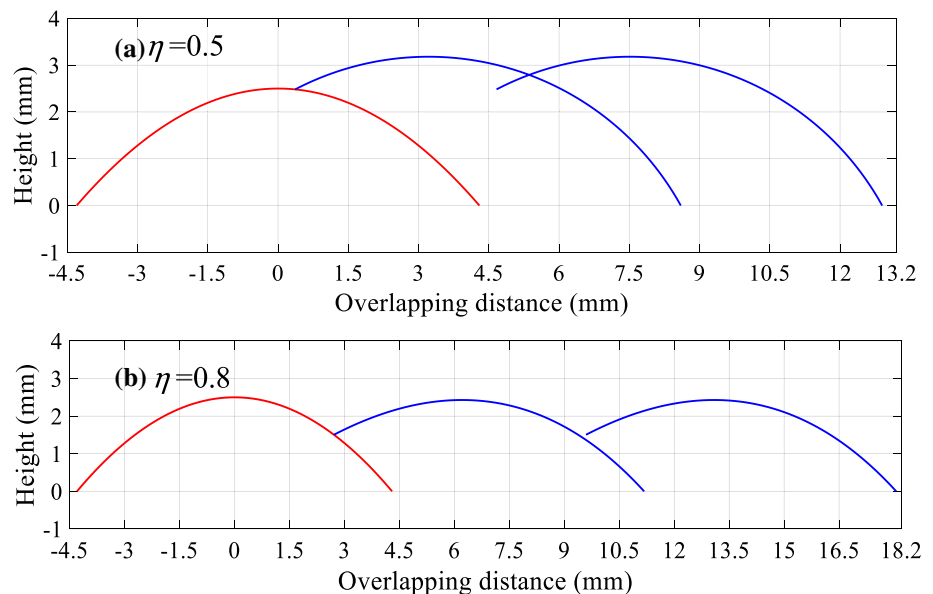
profile would be unsuitable to express the third one. As is shown in Fig. 13b, the profiles were not connected and a gap appeared in the valley between the second and third bead. Overall, when the overlapping ratio $\eta < \eta_b$ or $\eta > \eta_b$, the top flatness of the deposited layer was fluctuated significantly, and the overlapping process was not stable.

Besides, the flatness of the layer top surface with different overlapping ratio was further evaluated. The variance of the height value was calculated as is expressed by Eq. (12), which could reveal the fluctuation and the flatness of the top surface.

$$\sigma^2 = \frac{(h_1 - \mu)^2 + (h_v - \mu)^2 + (h_2 - \mu)^2}{3} \quad (12)$$

where h_1 was the peak height of the first bead, h_v was the height of the first valley, h_2 was the peak height of the second bead, μ was the mean value of the height, and σ^2 was the variance. The height variance for different overlapping ratio from 0.4 to 0.8 was calculated as is shown in Fig. 14. The variance value decreased firstly and increased gradually with the increasing of the overlapping ratio, and it can be observed that the variance value ($\sigma^2 = 0.0593$) at the optimal overlapping ratio ($\eta_b = 0.6557$) was at the bottom of the curve, indicating that the fluctuation of the height value was small and the flatness of the top surface was relatively good. Therefore, the flat layer surface and the stable overlapping process could be achieved through the calculated optimal overlapping ratio.

Moreover, the optimal overlapping distance for different bead geometry was also investigated. Firstly, a group of geometrical parameters was selected, in which the width and height increase with the same scale so that the width-height ratio (w/h, WHR) remains unchanged. It was found that the optimal overlapping distance remains unchanged for the
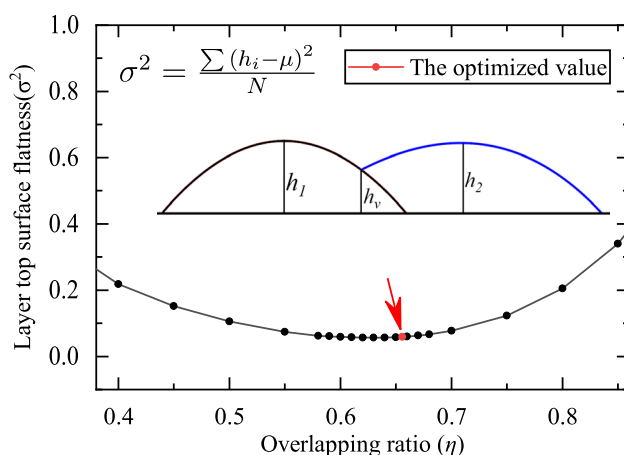
same width-height ratio. Another group of parameters was also calculated that the width-height ratio increased from 2.4 to 20, and the optimal overlapping ratio was shown in Fig. 15. It was observed that the optimal overlapping ratio decreased drastically and then reached a steady state with the increasing of the width-height ratio. The curve was fitted through the Eq. (13), where a, b, c and d were the coefficients, the R^2 was 0.9994, and the $RSME$ was 6.11×10^{-4}, which indicated that the equation could represent the nonlinear relationship between the optimal overlapping ratio and the WHR with high accuracy. For the selected parameters, the WHR = 3.44, $\eta_b = 0.6557$. For the gas metal arc welding with the experimental conditions described in this paper, through several preliminary experiments, the width-height ratio for the majority of beads was found lying in the region [2.5, 5], and the optimal overlapping ratio lay in the region [0.6317, 0.7732], obtained through the fitted function. Therefore, the optimal overlapping ratio decreased with the
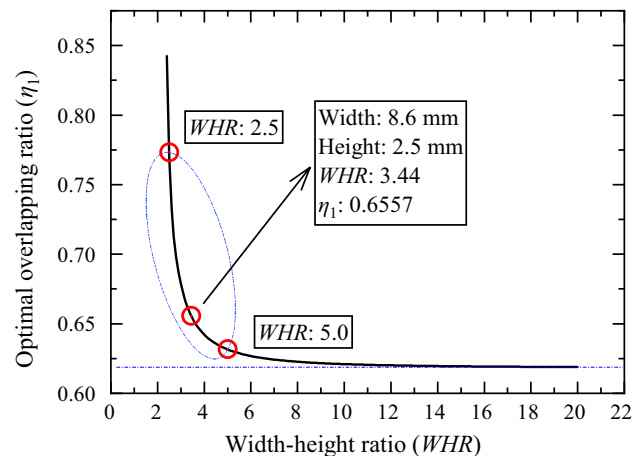
Fig. 15 The optimal overlapping ratio with different width-height ratio

Table 2 The welding parameters for validation experiment with different WHR

No.	1	2	3
Wire feed speed (WFS, m/min)	6.5	5.0	5.0
Arc voltage (AV, V)	23.0	22.2	23.0
Troch travel speed (TTS, mm/s)	4.0	6.0	6.0
Contact tip to workpiece distance (CTWD, mm)	8.0	8.0	8.0
Bead width (w, mm)	11.44	8.60	9.93
Bead height (h, mm)	3.77	2.50	2.38
Width-height ratio (WHR)	3.04	3.44	4.17
Tangency point (η_T)	0.5744	0.5841	0.5950
Optimal overlapping ratio (η_b)	0.6755	0.6557	0.6394

Fig. 14 The flatness (σ^2) of the layer top surface with different overlapping ratio

increasing of the weld bead width-height ratio, and it could be predicted through the fitted function.

$$y = \frac{ax^b}{x+c} + d, \quad x \in [2.4, \ 20], \quad x = w/h$$
$$a = 0.07548, \quad b = -0.3635, \quad c = -2.154, \quad d = 0.6169 \tag{13}$$

Results of validation experiment and discussion

To valid the multi-bead overlapping model and the optimal overlapping distance, three groups of experiment with different width-height ratio (WHR) were performed according to Fig. 15, as is listed in Table 2. The WHR and welding parameters in No. 2 was remained consistent with the preliminary experiment. The WHR in No. 1 and No. 3 was different form No. 2, which could valid the fitness of the VOM model with different welding parameters and WHR. The optimal overlapping ratio was calculated with the VOM model based on the parameters. According to the proposed TOM method (Ding et al. 2015), the optimal overlapping ratio should be 0.738, which exceeded the optimal value for the proposed VOM method in this paper, and would result in a uneven layer surface. Therefore, three experiments with the overlapping ratio 0.5, 0.738 and the respective optimal overlapping ratio were performed in each group.

To avoid the influence of heat accumulation, the substrate was cooled down to the ambient temperature before the deposition of the next bead. When $d_o = \eta_T w$, five beads were overlapped, to valid the proposed VOM model, the stable overlapping process and the layer flatness; When $d_o < \eta_T w$, two beads were overlapped, which was enough to valid the model and the unstable overlapping process; When $d_o \geq \eta_T w$, three beads were overlapped, which made it convenient to

observe the remarkable unevenness of the layer caused by the excessively large overlapping distance. The bead length was 70 mm, and the overlapping beads for different overlapping ratio in group No. 2 is shown in Fig. 16, and the figure (d, e, f) was the respective cross section.

The bead cross-section profile of the multi-bead overlapping experiment with different overlapping distance was measured through the 3D laser scanner and extracted as is shown in Fig. 17. The predicted curve and the actual welding bead profile were aligned and compared to evaluate the goodness of the proposed model. The point on actual bead profile was $S(x_i)$, $i \in [1, m]$, the point on predicted curve was $Q(x_j)$, $j \in [1, n]$, and the discrete Hausdorff distance (Chen et al. 2010) between the predicted and actual curve was calculated through the following equation:

$$e_i = \min_{1 \leq j \leq n} \left(Q(x_i) - S(x_j) \right) \tag{14}$$

where e_i was the minimum distance of the point on the actual bead profile to the overall predicted curve, which could reveal the approximation degree of the predicted curve and the actual bead profile. Figure 18 showed the curve distance of the three groups for $\eta = 0.5$, $\eta = $ Optimal value, and $\eta = 0.738$. The maximum distance and the average distance for the three groups of experiment with different WHR were listed in Table 3. The average distance was less than 0.28 mm, while the maximum distance was less than 0.73 mm for different welding process parameters, bead geometry and overlapping ratio. It revealed that the predicted cross-section curve could approximate the actual bead profile with a high accuracy at different overlapping ratio, which indicated that the proposed varying profile multi-bead overlapping model (VOM) was in good agreement with the actual forming principle of the multi-bead overlapping process, and the model could fit different welding parameters.

For group No. 2, the bead profile with the optimal overlapping distance was shown in Fig. 17a, and it can be found

Fig. 16 The multi-bead overlapping experiment of group No. 2

(a) $\eta = 0.5$ **(b)** $\eta = 0.6557$ **(c)** $\eta = 0.738$ **(d)** **(e)** **(f)**

10 mm

20 mm
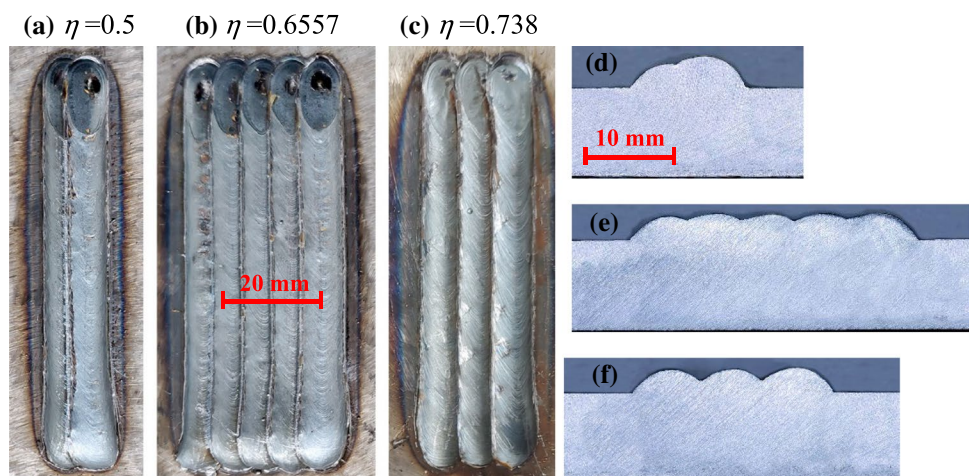
Fig. 17 Cross-section profile of the multi-bead overlapping experiment with different distance for group No. 2
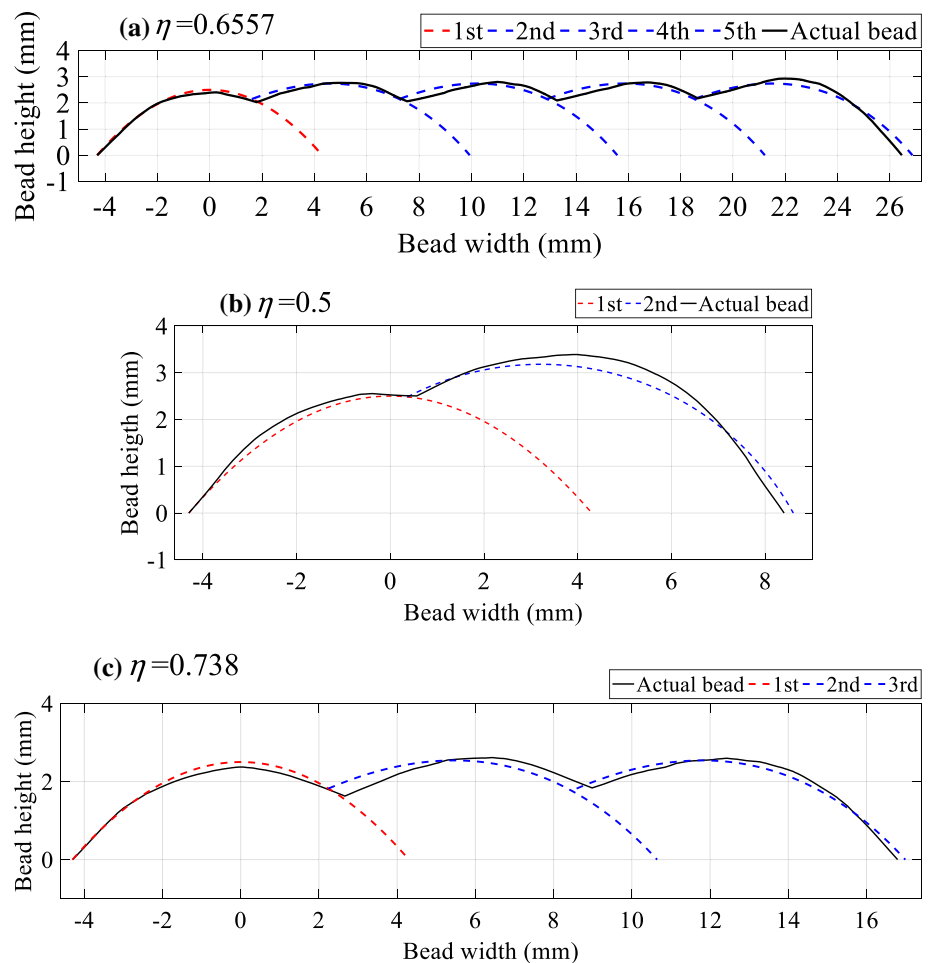
that the valley between the adjacent beads was shallow and the profile of the subsequent bead was consistent and stable, which indicated that the calculated optimal overlapping distance could achieve a flat deposited layer. The bead profile of $\eta = 0.5$ was illustrated in Fig. 17b, the second bead was almost heaped up on the first one, forming a convex hull, and the shape of the second bead was similar to the predicted profile with some error, which may be caused by the welding spatter and the measurement error. The profile of $\eta = 0.738$ was depicted in Fig. 17c, the forming characteristics was in consistent with the model, and the valley between the adjacent beads was much larger than that of the optimal overlapping distance, which would result in the uneven layer top surface. In addition, the forming characteristics of group No. 1 and No. 3 was similar to that of No. 2.

The top surface flatness of the welding layer for different *WHR* and overlapping ratio in group No. 1 to 3 was also calculated through the Eq. (12). As is shown in Fig. 19, with the increasing of the overlapping ratio, the layer flatness indicator decreased firstly and then increased, and the layer flatness at the optimal overlapping ratio was the best for the selected three groups with different *WHR*. When $\eta = 0.5$,

the overlapping ratio was less than the optimal value, the convex hull appeared for the excessive material filling in the valley; when $\eta = 0.738$, the overlapping ratio exceeded the optimal value, the deep valley was generated, and thus the layer surface flatness was poor. It indicated that the good layer surface could be obtained through the optimal value calculated with the proposed VOM model.

Accordingly, the experiment results denoted that the proposed varying process multi-bead overlapping model (VOM) could predict the shape variation of the second bead for different *WHR* and welding parameters well, and the flat layer surface could be achieved through the calculated optimal overlapping distance ratio. Besides, through the VOM model, the second bead shape could be quantitatively predicted without actual experiment or the complicated CFD simulations costing extensive computing resource and time, which would be significant to the research into the appearance optimization in additive manufacturing.

In this paper, the model with the constant overlapping ratio in a layer was developed, and for the future work, the model with the adaptive overlapping ratio could be considered, through which the different layer thickness in one layer

Fig. 18 The distance between the predicted curve and the actual experimental bead profile

(a) No.1, *WHR*=3.04

(b) No.2, *WHR*=3.44

(c) No.3, WHR=4.17
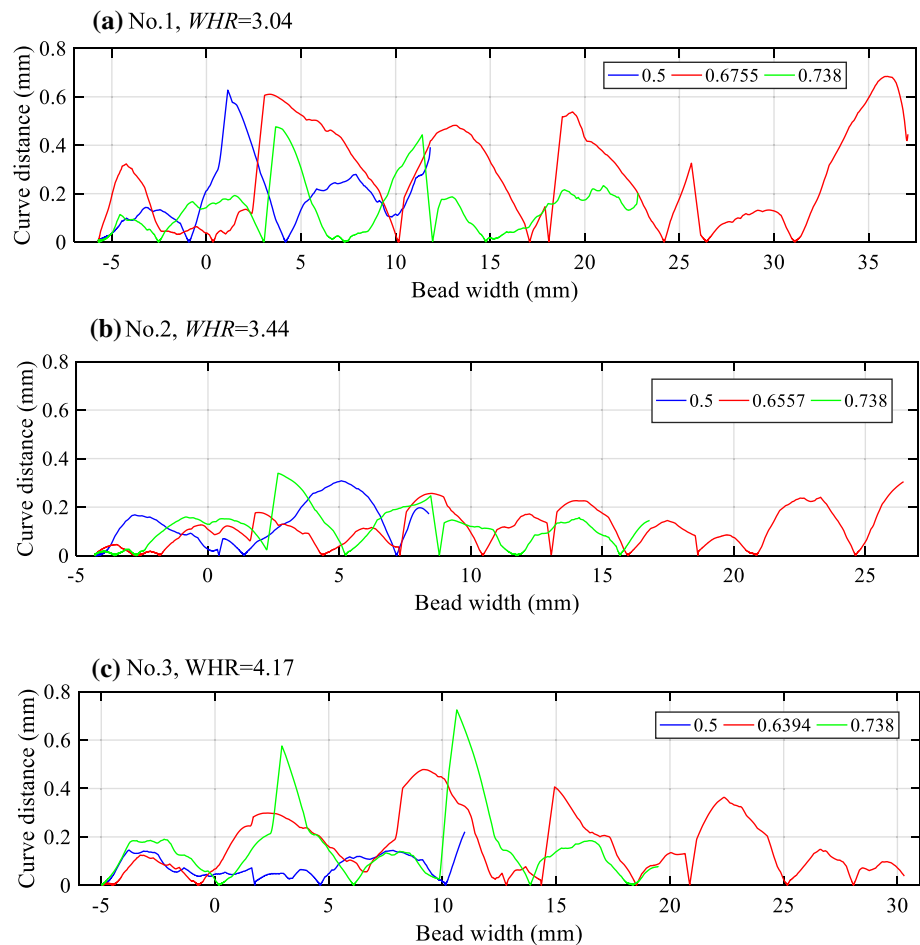
Table 3 The distance between the predicted curve and the actual bead profile

Overlapping ratio	0.5		Optimal		0.738	
Curve distance	Maximum	Average	Maximum	Average	Maximum	Average
No. 1	0.6276	0.1911	0.6842	0.2753	0.476	0.1433
No. 2	0.3086	0.1307	0.3045	0.1136	0.3399	0.1134
No. 3	0.2213	0.0786	0.4782	0.1642	0.7248	0.1638
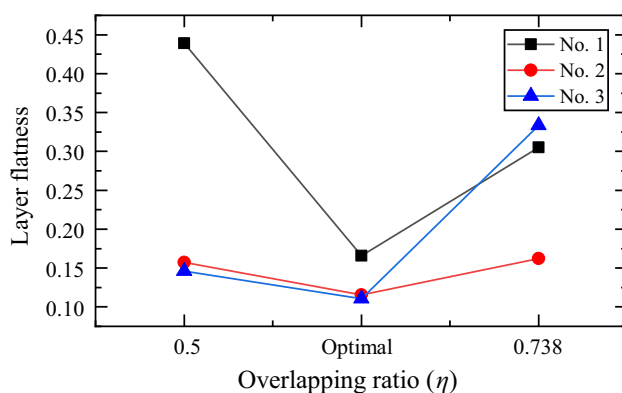
Fig. 19 The layer top surface flatness for different overlapping ratio

could be obtained. To search for the optimal overlapping ratio, the intelligent algorithm, such as the Taguchi method, the response surface method (RSM) or the genetic algorithm could be adapted, which would be effective to find the optimal configuration for the multiple process parameters. Additionally, the mechanical properties are nonnegligible issues for the GMAW-based additive manufacturing, and some attention could be devoted to the optimization of the mechanical properties and the avoidance of the welding defects.

Conclusion

To obtain a flat deposition layer in robotic GMAW-based additive manufacturing technology, a group of two-bead overlapping experiments was conducted, and the bead cross-section profile characteristics of the first and second bead in a layer were investigated. A varying profile multi-bead overlapping model (VOM) in GMAW-based additive manufacturing was proposed, and the optimal overlapping distance was calculated. The conclusions could be drawn as follows:

For the gas metal arc welding process, the cross-section profile of a single bead could be approximated by the parabola function with high accuracy. The profile of the second bead changed gradually with the overlapping distance, because of the damming up effect of the first bead. When the overlapping distance exceeded the tangency point ($\eta \geq \eta_T$), the profile of the second bead could be fitted by another parabola function with a rotated orientation; when the overlapping distance was less than the tangency point ($\eta < \eta_T$), the second bead profile could be fitted by a circular arc function. The chord length of the second bead profile remained unchanged for the different overlapping ratio. The multi-bead overlapping model with varying cross-section profile of adjacent bead could predict the second bead profile and reveal the changing process of different overlapping distance without the actual experiment. The optimal overlapping ratio varied with different geometrical parameters, and reduced with the increasing of the width-height ratio (*WHR*), which could be fitted with a custom nonlinear equation, and lay in the region [0.6317, 0.7732] for the different *WHR*. For the optimal overlapping ratio, the profile of the subsequent bead remained consistent, the overlapping process was stable, and the flatness of the layer top surface was relatively good. When $\eta < \eta_b$, the bead height would increase gradually, which would result in the declining layer surface; when $\eta > \eta_b$, the valley between the adjacent beads would be significant, leading to the wavy layer surface.

References

Arvo, J. (1992). Fast random rotation matrices. In *Graphics gems III (IBM version)* (pp. 117–120). Elsevier. https://doi.org/10.1016/b978-0-08-050755-2.50034-8.

Bai, X., Colegrove, P., Ding, J., Zhou, X., Diao, C., Bridgeman, P., et al. (2018). Numerical analysis of heat transfer and fluid flow in multilayer deposition of PAW-based wire and arc additive manufacturing. *International Journal of Heat and Mass Transfer, 124,* 504–516. https://doi.org/10.1016/j.ijheatmasstransfer.2018.03.085.

Cao, Y., Zhu, S., Liang, X., & Wang, W. (2011). Overlapping model of beads and curve fitting of bead section for rapid manufacturing by robotic MAG welding process. *Robotics and Computer-Integrated Manufacturing, 27*(3), 641–645. https://doi.org/10.1016/j.rcim.2010.11.002.

Chen, X.-D., Ma, W., Xu, G., & Paul, J.-C. (2010). Computing the Hausdorff distance between two B-spline curves. *Computer-Aided Design, 42*(12), 1197–1206. https://doi.org/10.1016/j.cad.2010.06.009.

Cho, D.-W., Park, J.-H., & Moon, H.-S. (2019). A study on molten pool behavior in the one pulse one drop GMAW process using computational fluid dynamics. *International Journal of Heat and Mass Transfer, 139,* 848–859. https://doi.org/10.1016/j.ijheatmasstransfer.2019.05.038.

Cunningham, C. R., Flynn, J. M., Shokrani, A., Dhokia, V., & Newman, S. T. (2018). Invited review article: Strategies and processes for high quality wire arc additive manufacturing. *Additive Manufacturing, 22,* 672–686. https://doi.org/10.1016/j.addma.2018.06.020.

Ding, D., Pan, Z., Cuiuri, D., & Li, H. (2015). A multi-bead overlapping model for robotic wire and arc additive manufacturing (WAAM). *Robotics and Computer-Integrated Manufacturing, 31,* 101–110. https://doi.org/10.1016/j.rcim.2014.08.008.

Ding, Y., Akbari, M., & Kovacevic, R. (2018). Process planning for laser wire-feed metal additive manufacturing system. *The International Journal of Advanced Manufacturing Technology, 95*(1–4), 355–365. https://doi.org/10.1007/s00170-017-1179-z.

Ghanty, P., Paul, S., Mukherjee, D. P., Vasudevan, M., Pal, N. R., & Bhaduri, A. K. (2007). Modelling weld bead geometry using neural networks for GTAW of austenitic stainless steel. *Science and Technology of Welding and Joining, 12*(7), 649–658. https://doi.org/10.1179/174329307X238399.

Gu, D. D., Meiners, W., Wissenbach, K., & Poprawe, R. (2012). Laser additive manufacturing of metallic components: Materials, processes and mechanisms. *International Materials Reviews, 57*(3), 133–164. https://doi.org/10.1179/1743280411Y.0000000014.

Hu, J., Guo, H., & Tsai, H. L. (2008). Weld pool dynamics and the formation of ripples in 3D gas metal arc welding. *International Journal of Heat and Mass Transfer, 51*(9–10), 2537–2552. https://doi.org/10.1016/j.ijheatmasstransfer.2007.07.042.

Hu, Z., Qin, X., Shao, T., & Liu, H. (2018). Understanding and overcoming of abnormity at start and end of the weld bead in additive manufacturing with GMAW. *The International Journal of Advanced Manufacturing Technology, 95*(5–8), 2357–2368. https://doi.org/10.1007/s00170-017-1392-9.

Jhavar, S., Jain, N. K., & Paul, C. P. (2014). Development of micro-plasma transferred arc (μ-PTA) wire deposition process for additive layer manufacturing applications. *Journal of Materials Processing Technology, 214*(5), 1102–1110. https://doi.org/10.1016/j.jmatprotec.2013.12.016.

Jiang, J., Hu, G., Li, X., Xu, X., Zheng, P., & Stringer, J. (2019a). Analysis and prediction of printable bridge length in fused deposition modelling based on back propagation neural network. *Virtual and Physical Prototyping, 14*(3), 253–266. https://doi.org/10.1080/17452759.2019.1576010.

Jiang, J., Stringer, J., & Xu, X. (2019b). Support optimization for flat features via path planning in additive manufacturing. *3D Printing and Additive Manufacturing, 6*(3), 171–179. https://doi.org/10.1089/3dp.2017.0124.

Las-Casas, M. S., de Ávila, T. L. D., Bracarense, A. Q., & Lima, E. J. (2018). Weld parameter prediction using artificial neural network: FN and geometric parameter prediction of austenitic stainless steel welds. *Journal of the Brazilian Society of Mechanical*

Sciences and Engineering, 40(1), 26. https://doi.org/10.1007/s40430-017-0928-0.

Lei, Y., Xiong, J., & Li, R. (2018). Effect of inter layer idle time on thermal behavior for multi-layer single-pass thin-walled parts in GMAW-based additive manufacturing. *The International Journal of Advanced Manufacturing Technology, 96*(1–4), 1355–1365. https://doi.org/10.1007/s00170-018-1699-1.

Li, Y., Han, Q., Zhang, G., & Horváth, I. (2018). A layers-overlapping strategy for robotic wire and arc additive manufacturing of multi-layer multi-bead components with homogeneous layers. *The International Journal of Advanced Manufacturing Technology, 96*(9–12), 3331–3344. https://doi.org/10.1007/s00170-018-1786-3.

Panda, B., Shankhwar, K., Garg, A., & Savalani, M. M. (2019). Evaluation of genetic programming-based models for simulating bead dimensions in wire and arc additive manufacturing. *Journal of Intelligent Manufacturing, 30*(2), 809–820. https://doi.org/10.1007/s10845-016-1282-2.

Prajadhiama, K. P., Manurung, Y. H., Minggu, Z., Pengadau, F. H., Graf, M., Haelsig, A., et al. (2019). Development of bead modelling for distortion analysis induced by wire arc additive manufacturing using FEM and experiment. *MATEC Web of Conferences, 269,* 05003. https://doi.org/10.1051/matecconf/201926905003.

Roberts, I. A., Wang, C. J., Esterlein, R., Stanford, M., & Mynors, D. J. (2009). A three-dimensional finite element analysis of the temperature field during laser melting of metal powders in additive layer manufacturing. *International Journal of Machine Tools and Manufacture, 49*(12–13), 916–923. https://doi.org/10.1016/j.ijmachtools.2009.07.004.

Sheng, Z., Yuan, G., & Cui, Z. (2018). A new adaptive trust region algorithm for optimization problems. *Acta Mathematica Scientia, 38*(2), 479–496. https://doi.org/10.1016/S0252-9602(18)30762-8.

Suryakumar, S., Karunakaran, K. P., Bernard, A., Chandrasekhar, U., Raghavender, N., & Sharma, D. (2011). Weld bead modeling and process optimization in hybrid layered manufacturing. *Computer-Aided Design, 43*(4), 331–344. https://doi.org/10.1016/j.cad.2011.01.006.

Weng, F., Gao, S., Jiang, J., Wang, J., & Guo, P. (2019). A novel strategy to fabricate thin 316L stainless steel rods by continuous directed energy deposition in Z direction. *Additive Manufacturing, 27,* 474–481. https://doi.org/10.1016/j.addma.2019.03.024.

Williams, S. W., Martina, F., Addison, A. C., Ding, J., Pardal, G., & Colegrove, P. (2016). Wire + arc additive manufacturing. *Materials Science and Technology, 32*(7), 641–647. https://doi.org/10.1179/1743284715Y.0000000073.

Xiong, J., Zhang, G., Gao, H., & Wu, L. (2013). Modeling of bead section profile and overlapping beads with experimental validation for robotic GMAW-based rapid manufacturing. *Robotics and Computer-Integrated Manufacturing, 29*(2), 417–423. https://doi.org/10.1016/j.rcim.2012.09.011.

Xiong, X., Zhang, H., & Wang, G. (2009). Metal direct prototyping by using hybrid plasma deposition and milling. *Journal of Materials Processing Technology, 209*(1), 124–130. https://doi.org/10.1016/j.jmatprotec.2008.01.059.

Yang, D., He, C., & Zhang, G. (2016). Forming characteristics of thin-wall steel parts by double electrode GMAW based additive manufacturing. *Journal of Materials Processing Technology, 227,* 153–160. https://doi.org/10.1016/j.jmatprotec.2015.08.021.

Zhang, Y., Bernard, A., Harik, R., & Karunakaran, K. P. (2017). Build orientation optimization for multi-part production in additive manufacturing. *Journal of Intelligent Manufacturing, 28*(6), 1393–1407. https://doi.org/10.1007/s10845-015-1057-1.

Zheng, X., Cheng, K., Zhou, X., Lin, J., & Jing, X. (2018). An adaptive direct slicing method based on tilted voxel of two-photon polymerization. *The International Journal of Advanced Manufacturing Technology, 96*(1–4), 521–530. https://doi.org/10.1007/s00170-017-1507-3.

Zhou, X., Zhang, H., Wang, G., & Bai, X. (2016). Three-dimensional numerical simulation of arc and metal transport in arc welding based additive manufacturing. *International Journal of Heat and Mass Transfer, 103,* 521–537. https://doi.org/10.1016/j.ijheatmasstransfer.2016.06.084.

Springer

Terms and Conditions